Journal of Applied Physics ARTICLE scitation.org/journal/jap

Magnetotransport and superconductivity in InBi films grown on Si(111) by molecular beam epitaxy

Cite as: J. Appl. Phys. **126**, 103901 (2019); doi: 10.1063/1.5109542
Submitted: 9 May 2019 · Accepted: 15 August 2019 ·
Published Online: 9 September 2019

Phillip Dang,[1,a)] Sergei Rouvimov,[2] Huili Grace Xing,[3,4,5] and Debdeep Jena[3,4,5,b)]

AFFILIATIONS

[1]School of Applied and Engineering Physics, Cornell University, Ithaca, New York 14853, USA
[2]Department of Electrical Engineering, University of Notre Dame, Notre Dame, Indiana 46556, USA
[3]School of Electrical and Computer Engineering, Cornell University, Ithaca, New York 14853, USA
[4]Department of Materials Science and Engineering, Cornell University, Ithaca, New York 14853, USA
[5]Kavli Institute at Cornell for Nanoscale Science, Cornell University, Ithaca, New York 14853, USA

Note: This paper is part of the Special Topic on Highly Mismatched Semiconductors Alloys: From Atoms to Devices.
[a)]**Electronic mail:** pd382@cornell.edu
[b)]**Electronic mail:** djena@cornell.edu

ABSTRACT

Bismuth-containing compounds inherit the high spin-orbit coupling and bandgap bowing effects of the Bi atom. Here, we report the growth of InBi films using molecular beam epitaxy. By growing in a Bi-rich regime, we obtain coalesced and crystalline films with a sharp interface to the high-resistivity Si(111) substrate. Temperature-dependent transport and resistivity measurements exhibit a nonlinear Hall effect and parabolic magnetoresistance, suggesting two-carrier semimetallic behavior. In In-rich films, metallic temperature-dependent resistivity is observed. In Bi-rich films, we observed semiconductorlike temperature-dependent resistivity as well as superconductivity.

I. INTRODUCTION

Bismuth-containing compounds and alloys have historically been well-studied materials due to the heavy-atom effects of bismuth and are garnering increasing interest. In 1930, the unique electronic structure of pure Bi allowed for the discovery of the Shubnikov-de Haas[1] and de Haas-van Alphen effects.[2] Bi-based compounds, such as Bi_2Se_3, Bi_2Te_3, and $Bi_{1-x}Sb_x$, later became very popular materials for thermoelectrics due to the heavy Bi element and narrow bandgaps.[3] Heavy elements increase phonon scattering, which decreases thermal conductivity, while narrow bandgaps increase electrical conductivity. Low thermal conductivity and high electrical conductivity are necessary to maximize the ZT figure of merit for thermoelectric materials. Such Bi-based compounds and their alloys were found to be topological insulators and have seen applications in spintronics and spin-orbitronics.[4–6] Even for Bi-based materials that are not topological insulators, the large spin-orbit coupling has led to large spin polarization effects, such as that seen in CuBi.[7]

The heavy-atom effects of Bi also make it appealing to integrate into III-V semiconductors. Epitaxial growth of III-V materials and heterostructures has seen great success in the past few decades with semiconductors such as GaN, InP, GaAs, and InSb being the subjects of countless research topics and commercial devices. Bi is the heaviest stable group V element, in the same column as N, P, As, and Sb in the period table. The contribution of bismuth to epitaxial III-V materials has mainly been in the form of dilute bismide alloys.[8] When alloyed into a III-V semiconductor, bismuth produces a large bandgap bowing effect by significantly reducing the bandgap of the semiconductor with only dilute amounts of bismuth incorporation.[9] This is analogous to the dilute nitrides, where dilute amounts of nitrogen incorporation into GaAs lowers the bandgap[10,11] by decreasing the conduction band minimum.[12] Bismuth, on the other hand, decreases the bandgap of a III-V semiconductor by increasing the valence band minimum.[13] This bandgap bowing effect, in addition to large spin-orbit coupling, has made bismuth an element of high interest for alloying in the III-phosphide,[14,15] III-arsenide,[9,16–20] and III-antimonide[21,22] material families in order to tune the bandgap for infrared photonic device applications. However, III-Bi *binary* compounds have been

relatively unexplored. To understand the properties of the dilute bismide ternary alloys, the binary extremum, where Bi completely replaces the other group V material, is of significant interest.

InBi has recently been theoretically predicted to be a potential topological insulator,[23–29] an efficient spin Hall material,[30] and a topological semimetal.[31,32] Experimentally, InBi has been identified as a possible topological crystalline insulator,[29] topological semimetal,[31] and superconductor.[33–37] However, InBi has previously only been grown in the bulk crystal form,[31,36–38] as uncoalesced thin films,[39] or as a single or interfacial layer.[29,40,41] Previous attempts of growing InBi epitaxially as a thin film led to heavy droplet formation and lack of coalescence.[39] In this work, we obtain conditions for molecular beam epitaxial growth of coalesced InBi films on high-resistivity Si (111) substrates. Subsequent magnetotransport measurements on the films reveal nonlinear Hall effect and superconductivity.

II. METHODS

The InBi epitaxial films were grown in a Veeco Gen Xplor molecular beam epitaxy (MBE) system on high-resistivity Si(111) substrates. Silicon substrates are nonpolar and cubic while having a smaller lattice constant than III-V semiconductors, making them promising for demonstrating that coalesced InBi can grow on a widespread semiconductor platform. Si(111) was also predicted to be ideal substrates for realizing nontrivial topological behavior in InBi.[25,40,41] A dual-filament hot-lip effusion cell was used for 7N pure indium flux, and a standard Knudsen effusion cell was used for 6N pure bismuth flux. Elemental fluxes were measured as beam-effective pressures (BEPs) by a nude Baynard-Alpert ion gauge, and cell temperatures were measured by thermocouples. A BEP of about 10^{-6} Torr of bismuth, corresponding to a cell temperature of 600 °C, was used for all growths. The indium BEP was varied from 2.19–5.50 × 10^{-7} Torr, corresponding to temperatures of 816–858°C on the cell tip and 716–758°C on the cell base. The growth rates of the InBi films were at least 7.8 nm/min depending on the indium flux. A table of the samples studied in this paper is shown in Table I. *In situ* surface morphology was monitored by a reflection high-energy electron diffraction (RHEED) system from Staib instruments. Before growth, the Si(111) substrates were flashed at 1000–1200°C to desorb native oxides, and a 7 × 7 surface reconstruction was visible by RHEED upon cooling down. The substrate was left to cool to a thermocouple-measured growth temperature of 50 °C.

After growth, the films were characterized by X-ray diffraction (XRD), scanning electron microscopy (SEM), and magnetotransport. To further explore the structure of the films, transmission electron microscopy (TEM) was used. Cross-sectional energy-dispersive X-ray spectroscopy (EDS) was used in STEM mode to measure the indium and bismuth content as a function of depth in the film. By taking angle-dependent selected area diffraction (SAD) of the cross-section of the film, the crystal structure of the $InBi_x$ films were the determined.

Magnetotransport measurements were taken on a Quantum Design Physical Property Measurement System (PPMS). Van der Pauw contacts were placed on the grown films by soldering indium dots onto the corners of 1 × 1 cm^2 square samples. Electrical measurements were made with direct current using a Keithley 6220 current source and a Keithley 2182A nanovoltmeter. A Keithley 7001 system was used to switch between the Van der Pauw contacts for accurate Hall effect measurements.

III. RESULTS

A. Growth and structure

Initial MBE growths of InBi at substrate temperatures ranging from 200 to 500 °C resulted in uncoalesced droplets, which is in line with the report of Keen *et al.*[39] The RHEED screen during growth at these temperatures was completely dark, but *ex situ* XRD measurements revealed crystal peaks associated with Bi, In, InBi, and In_2Bi. This suggests that liquid droplets formed during the higher-temperature growths, and those droplets crystallized upon cooling to room temperature. The temperatures at which these initial growths were done cover the temperature range at which most III-V dilute bismides are grown. Therefore, growers of metal-rich, indium-containing dilute bismides may expect InBi droplet formation that crystallizes onto their films upon cooldown. For this study, however, we aim for coalesced films of InBi compound and proceed to lower-temperature growths.

By reducing the growth temperature to 50 °C, the droplets were observed to merge together to form films. Whether the films coalesced or not was found to depend on the Bi:In flux ratio. Coalescence of the samples increases with increased Bi:In flux, as seen in Figs. 1(a)–1(d). We attribute this to the melting points of the indium-bismuth eutectic system. The indium-bismuth phase diagram[42] shows that the melting point of the indium-bismuth system is lower than that of both indium and bismuth. As the bismuth content of an indium-bismuth melt is increased, the melting point increases. Films with higher Bi:In flux ratios should, therefore, have higher melting points.

TABLE I. List of MBE-grown InBi and Bi samples compared in this study.

Sample ID	Growth temperature (°C)	Bismuth BEP (10^{-7} Torr)	Indium BEP (10^{-7} Torr)	Bi:In BEP ratio	Growth duration (min)	Superconducting T_c (K)
A	50	9.97	5.50	1.81	60	…
B	50	9.96	4.66	2.14	60	…
C	50	9.67	3.91	2.47	60	…
D	50	10.6	2.19	4.84	60	2.28
E	150	15.5	…	∞	80	…

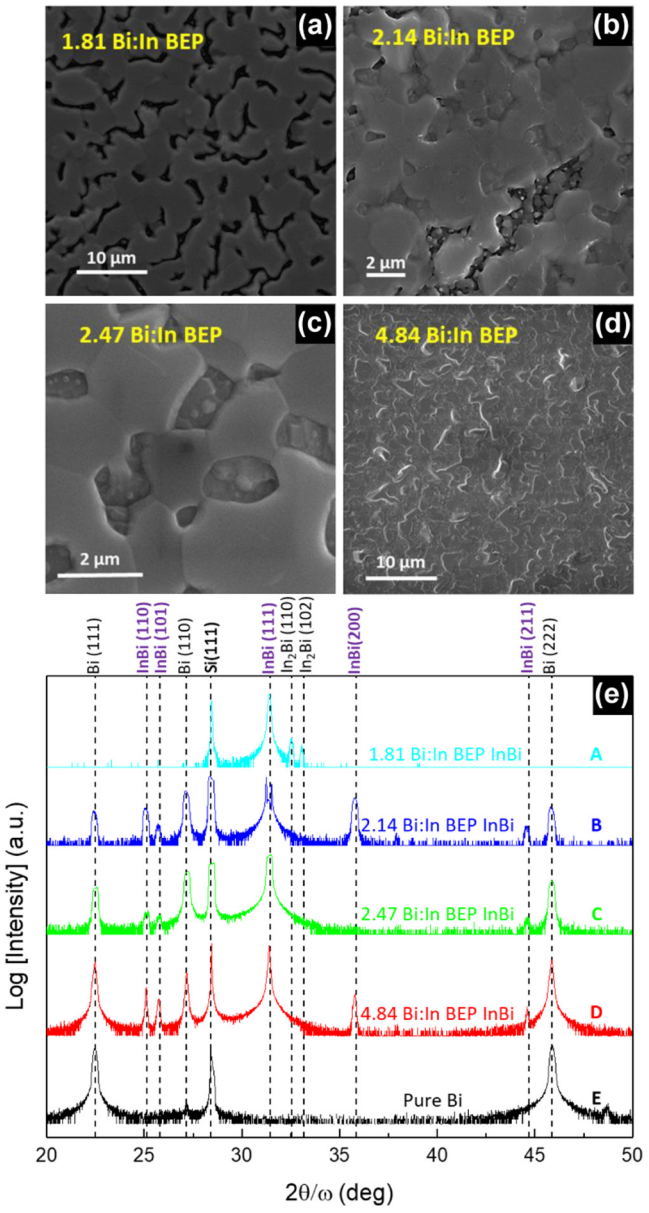

FIG. 1. Surface SEM images of > 500 nm thick indium-bismuth samples grown with Bi:In flux ratios of (a) Sample A, (b) Sample B, (c) Sample C, and (d) Sample D. Coalescence is seen to increase as the indium flux is lowered. (e) XRD of $InBi_x$ grown at different Bi:In flux ratios. Purple peak labels indicate XRD peaks of stoichiometric InBi. Samples from lowest to highest Bi:In flux ratios are labeled Samples A, B, C, D, and E, respectively (see Table I).

The crystalline compounds within the $InBi_x$ films were identified with XRD, as shown in Fig. 1(c). The four $InBi_x$ samples studied had Bi:In BEP ratios ranging from 1.81 to 4.84 and were labeled Samples A–D, respectively (see Table I). Sample E, a pure Bi sample, is shown for comparison and predominantly displays the Bi (111) and (222) peaks. We see that Samples B–D have inclusions of pure Bi crystallytes, and as Bi:In flux ratios decrease, the relative intensity of the pure Bi peaks decreases. The contribution of pure Bi decreases until no clear pure Bi peak can be seen for Sample A. For all $InBi_x$ samples, the InBi(111) peak is strongest, but for Samples B–D, peaks corresponding to the InBi (110), (101), (200), and (211) planes can be seen. For Sample A with the lowest Bi:In ratio, these additional InBi peaks are not seen, but contributions from the In_2Bi phase become apparent.

The different phases of indium-bismuth alloys that form could also be a contributing factor to the coalescence of the $InBi_x$ films. To further explore the phases within the film, we use TEM and cross-sectional EDS. Cross-sectional EDS, shown in Fig. 2, reveals that the film grown with 4.84 Bi:In BEP ratio (Sample D) is bismuth-rich with an average of 55.7% Bi and 44.3% In, while a film grown with 2.47 Bi:In BEP (Sample C) is indium-rich with an average of 37.1% Bi and 62.9% In. The TEM of these two coalesced samples are shown in Fig. 3. Sample D is highly crystalline and shows a sharp interface with the Si(111) substrate. Sample C, while also crystalline, shows more defects and a rougher interface. This roughness could potentially be due to etching of silicon due to excess indium. To confirm the structure of the two films, multiple SAD images were studied while rotating the film plane. The Bi-rich InBi layer of Sample D was found to have a tetragonal structure with an in-plane lattice constant of $a = 4.98$ Å and an out-of-plane lattice constant of $c = 4.81$ Å. The structure and lattice constants are in agreement with the expected values ($a = 5.015$ Å, $c = 4.771$ Å)[43] for the most stable tetragonal phase of InBi. However, the Sample C is found to have a hexagonal structure with an in-plane lattice constant of $a = 5.48$ Å and an out-of-plane lattice constant of $c = 6.54$ Å, which is in agreement with the expected hexagonal structure and lattice constants ($a = 5.455$ Å, $c = 6.502$ Å)[44] for In_2Bi.

Despite the clear indications of In_2Bi in Sample C (In-rich) under cross-sectional TEM, cross-sectional EDS, and selected area diffraction, measurements of XRD showed strong evidence of near-stoichiometric InBi. This puzzling behavior may be due to mixed InBi phases throughout the film when the Bi:In flux ratio is low

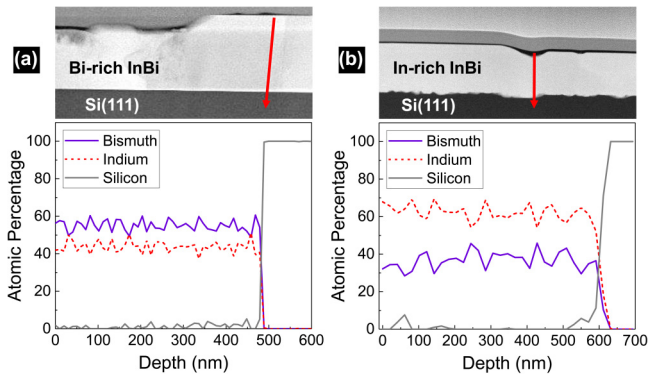

FIG. 2. Depth-dependent EDS measurement and corresponding TEM images of the In, Bi, and Si content of (a) Sample D and (b) Sample B.

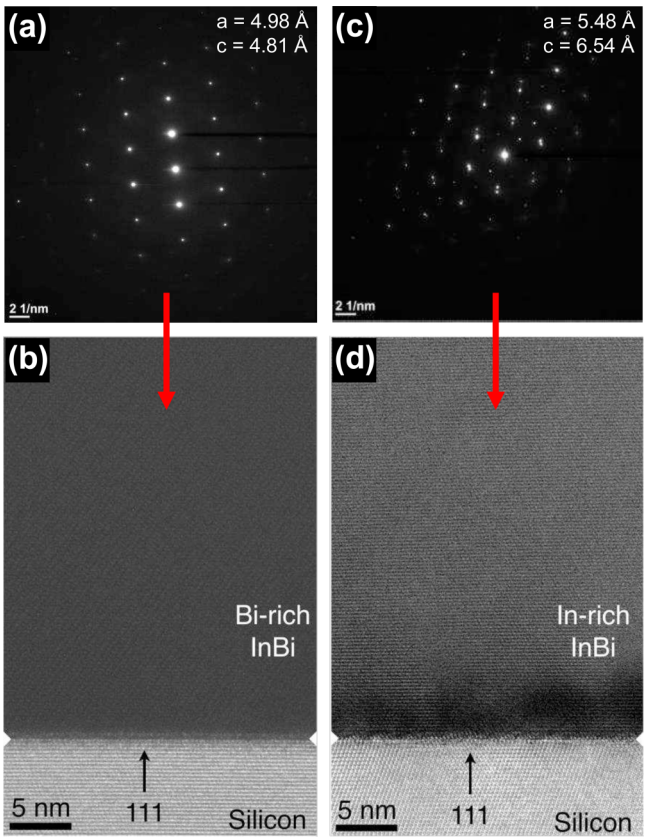

FIG. 3. (a) Selected area diffraction pattern and (b) cross-sectional TEM of Sample D with a Bi:In BEP ratio of 4.84. A sharp interface can be seen, and the SAD pattern shows the expected tetragonal phase of InBi. (c) Selected area diffraction pattern and (d) cross-sectional TEM of Sample B grown with a Bi:In BEP ratio of 2.14. The SAD pattern shows evidence of the hexagonal In_2Bi phase.

enough. This is supported by the appearance of mixed SAD patterns for Sample C, as shown in Fig. 3(c). The larger fluctuations in cross-sectional EDS atomic percentage for Sample C compared to Sample D (Bi-rich), as shown in Fig. 2, may also be indicative of phase mixing. However, such phase mixing within the crystallite analyzed by TEM does not fully account for how large the InBi peak seen by XRD was, so there could exist large crystals of InBi outside of the areas that were examined by TEM.

B. Magnetotransport properties

Magnetotransport measurements were taken on a pure Bi epitaxial film grown by MBE as the control sample (Sample E), the Bi-rich InBi sample (Sample D), and an In-rich InBi sample (Sample C). The Bi layer of Sample E was grown to be 500 nm thick by molecular beam epitaxy. Since those three samples were coalesced films on high-resisitivity Si(111) substrates, the charge transport occurs in the epitaxial layer and not the silicon. This is especially true for Sample D, which exhibits a sharp interface with the substrate. However, we acknowledge that the Bi crystallites in the InBi films that were previously detected by composition and structure measurements will also contribute to the transport properties of the InBi films. By comparing the InBi results to that of the control Bi sample and maintaining that the InBi properties, both structural and transport, overshadow the Bi properties in the InBi films, we aim to elucidate the transport properties of InBi.

The Hall effect and magnetoresistance (MR) curve shapes of the three samples show clear semimetallic behavior, indicated by the nonlinearity of the Hall effect and saturating magnetoresistance with B^2 dependence, as can be seen in Fig. 4. In general, pure Bi (Sample E) has a lower carrier concentration than Bi-rich InBi (Sample D), which has a lower concentration than In-rich InBi (Sample C). This can be immediately seen in Fig. 4(a), where the magnitude of ρ_{xy} varies significantly between the three samples. The transport data can be fit with the two-carrier model, given by the following equations:

$$\rho_{xx} = \frac{(n\mu_e + p\mu_h) + (n\mu_e\mu_h^2 + p\mu_e^2\mu_h)B^2}{e[(n\mu_e + p\mu_h)^2 + (n-p)^2\mu_e^2\mu_h^2B^2]}, \quad (1)$$

$$\rho_{xy} = \frac{(p\mu_h - n\mu_e)B + \mu_h^2\mu_e^2(p-n)B^3}{e[(n\mu_e + p\mu_h)^2 + (n-p)^2\mu_e^2\mu_h^2B^2]}, \quad (2)$$

where ρ_{xy} is the Hall resistivity, n is the electron concentration, p is the hole concentration, μ_e is the electron mobility, μ_h is the hole mobility, and B is the magnetic field. Due to the sensitivity of the fits when using two equations to fit four parameters, the individual mobilities of electrons and holes cannot be reliably reported. However, the total sum of carriers in each sample at room temperature can be extracted from the fits and plotted with conductivity, as shown in Fig. 5(a). The total carrier concentrations for Samples C, D, and E are 1.0×10^{22} cm^{-3}, 1.4×10^{21} cm^{-3}, and 3.4×10^{20} cm^{-3}, respectively. The conductivities and carrier concentrations of Samples D and E lie between those of semiconductors and metals, which is expected for semimetals. The carrier concentration of Sample C is comparable to that of common metals. The sensitivity of carrier concentration to $InBi_x$ composition may explain why extreme magnetoresistance is not seen in these samples despite being recently reported by Okawa *et al.*[45] Extreme magnetoresistance occurs in semimetals with nearly-compensated electron and hole concentrations, so additional carriers resulting from impurities and defects potentially masks the observation of extreme magnetoresistance in these samples.

The resistivity vs temperature is shown in Fig. 5(b). Samples D and E display semiconductorlike temperature dependence, indicative of resistivity dominated by the thermal activation of carriers. By fitting the resistivity vs temperature to an Arrhenius function, we obtain a thermal activation energy of 8.7 meV for Sample E and 10.2 meV for Sample D. On the other hand, Sample C shows metallic temperature dependence dominated by phonon scattering. This temperature-dependent behavior agrees with the observation that Sample C has a higher carrier concentration than Samples D and E. The temperature dependence of Sample C can be fitted to

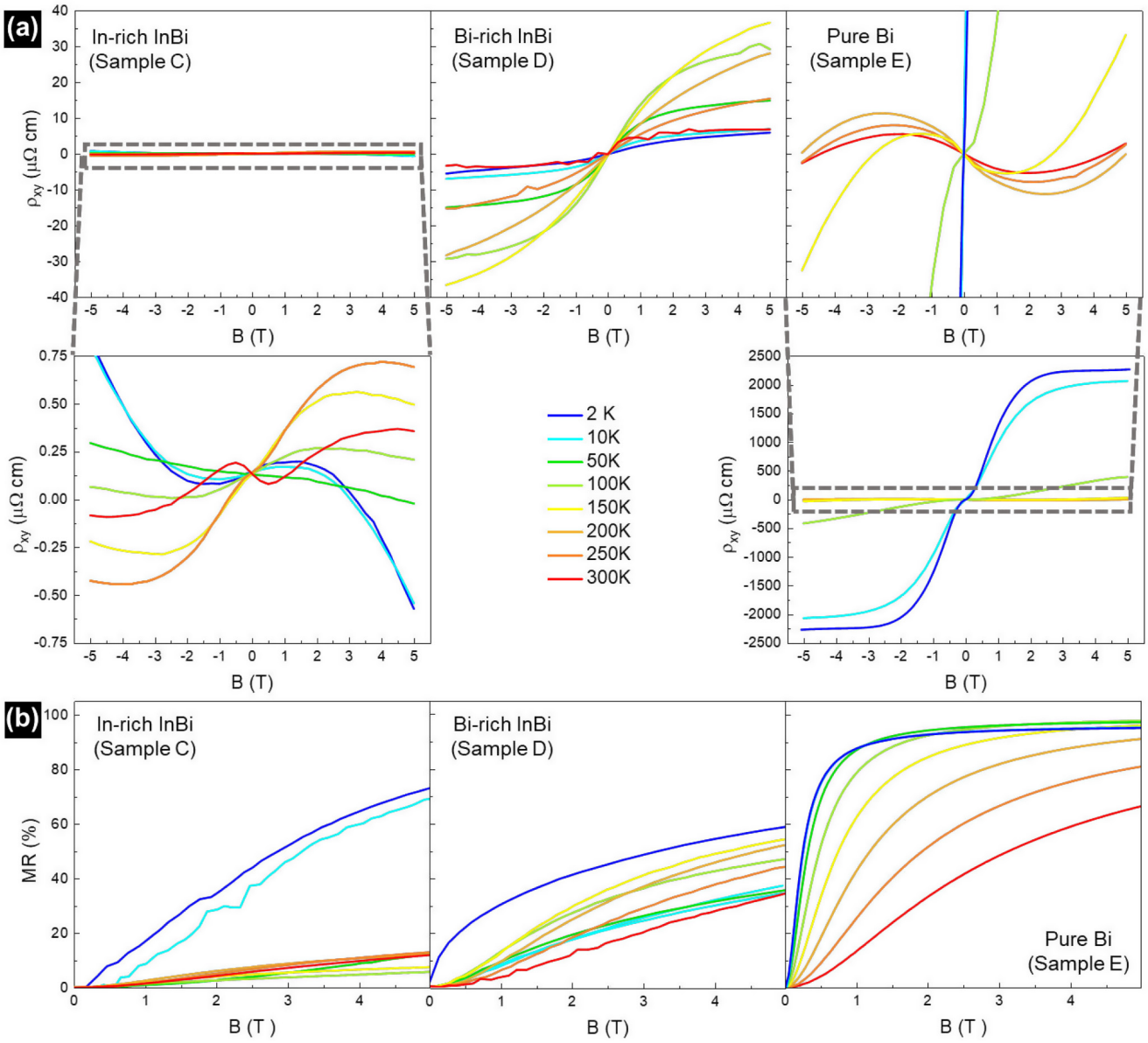

FIG. 4. (a) Hall effect and (b) magnetoresistance of In-rich InBi (Sample C), Bi-rich InBi (Sample D), and pure Bi (Sample E). In the second row, the plot is zoomed in for Sample C and zoomed out for Sample E in order to display the shape of the Hall effect.

Fermi liquid behavior, and the intercept of the fit allows us to extract a residual resistivity ratio (RRR) of 30.3. This RRR is rather low yet consistent with our TEM images in Fig. 2(a), which shows that Sample C has more defects and a rougher interface than Sample D. While a RRR for Sample D cannot be extracted from the semiconductorlike temperature dependence, we maintain from XRD, cross-sectional EDS, and TEM that the quality of Sample D is much higher than that of Sample C.

The magnitude of the magnetoresistance (MR) also shows an interesting difference between Samples C, D, and E. The MR percentage, which is shown in Fig. 5(b) at a magnetic field of 5 T and temperatures from 2 K to 300 K, is given by

$$MR = \frac{\rho_{xx}(B) - \rho_{xx}(0)}{\rho_{xx}(B)} \times 100\%, \tag{3}$$

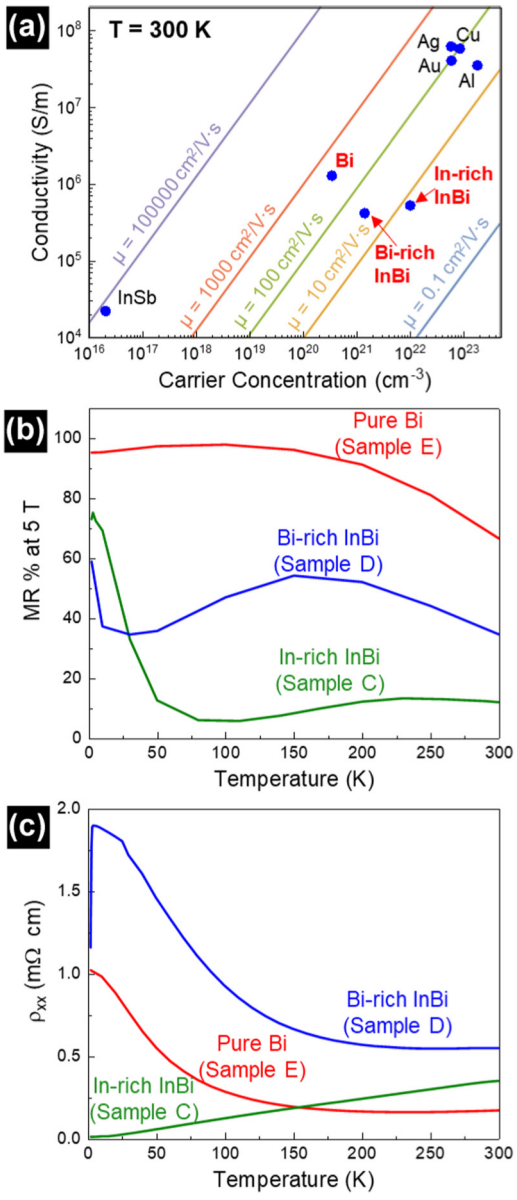

FIG. 5. (a) Conductivity vs carrier concentration of room temperature for MBE-grown In-rich InBi (Sample C), Bi-rich InBi (Sample D), and pure Bi (Sample E) compared to InSb and various metals. (b) Magnetoresistance of Samples C, D, and E at 5 T for various temperatures. Bi shows a nearly monotonic behavior. (c) Resistivity vs temperature of Samples C, D, and E.

where ρ_{xx} is the longitudinal resistivity. The temperature dependence of MR is quite simple for Sample E and almost monotonic. The band structure of pure Bi is fairly well-studied, and the Fermi surface of Bi(111) was shown to contain one electron pocket and six hole pockets.[46–48] The InBi samples (Samples C and D) show more complex temperature dependence, perhaps due to a more

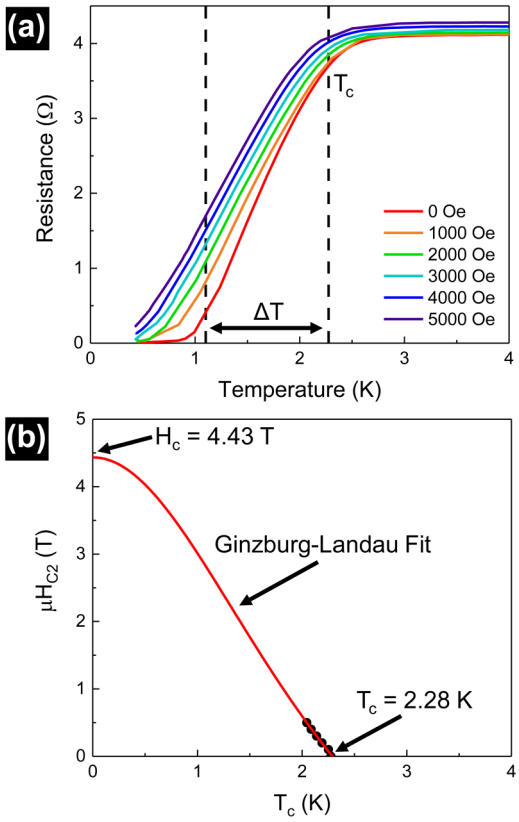

FIG. 6. (a) Resistances at low temperature for Bi-rich InBi (Sample D) at various fields between 0 and 5000 Oe. (b) Upper critical field vs critical temperature for Sample D. Black dots are experimental data extracted from the resistance vs temperature curves in (a), and the red line is a Ginzburg-Landau fit to the black dots.

complex Fermi surface. This would be in agreement with the theoretical calculations and photoelectron spectroscopy reports of Nicolai *et al.*[29] and Ekahana *et al.*,[31] which have discovered additional carrier pocket contributions and crossings in the band structure of InBi that are not present in pure Bi. In terms of MR magnitude, the three samples are somewhat comparable at low temperatures, but in general, pure Bi (Sample E) has larger MR than Bi-rich InBi (Sample D), which has larger MR than In-rich InBi (Sample C).

On the other hand, as shown in Fig. 6(a), the onset of superconductivity is visible with the sudden drop of ρ_{xx} at the lowest temperatures in Bi-rich InBi (Sample D). Temperature-dependent resistivity measurements were performed down to 0.45 K, using the He-3 option of the PPMS, to measure the superconducting critical temperature as a function of an external magnetic field. The results of these measurements are shown in Fig. 6. The critical temperature, T_c, was defined as the temperature at which resistance was 90% the resistance at 3.5 K, and the superconducting transition width, ΔT, is the temperature difference between resistances 90% and 10% of the

resistance at 3.5 K. That is, $T_c = T_c^{90\%}$ and $\Delta T = T_c^{90\%} - T_c^{10\%}$. For zero external magnetic field, a T_c of 2.28 K and a ΔT of 1.17 K were obtained. The superconductor is then quenched by magnetic fields between 0 and 5000 Oe, and the temperature-dependent resistance is plotted in Fig. 6(a). The T_c at each magnetic field is extracted and plotted in Fig. 6(b). The plot can then be fitted with the Ginzburg-Landau function

$$H_c(T) = H_c(0)\frac{1-(T/T_c)^2}{1+(T/T_c)^2}. \quad (4)$$

The fit indicates an upper critical field $H_c(0) \sim 4.43$ T. Previous studies have reported superconductivity in indium-rich indium-bismuth alloys, with T_c measured to be between 5.6 and 5.9 K for the In_2Bi phase and between 4.1 and 4.27 K for the In_5Bi_3 phase.[33,34,36,37] Gandhi *et al.* reported that in multiphase indium-bismuth alloys, the different critical temperatures of the phases resulted in a steplike descent to the zero-resistance superconducting state.[37] Since Sample D transitions to its superconducting state in one smooth step in Fig. 6(a), the superconductivity should be from a single dominant indium-bismuth phase. Pure indium has a $T_c \sim 3.4$ K, but no pure crystallites of indium were seen in Sample D through XRD or TEM. Pure bismuth crystallites were seen in Sample D by XRD, but the T_c of pure bismuth was measured to be much lower at 0.00053 K by Prakash *et al.*,[49] so pure bismuth cannot be responsible for the T_c measured here. Furthermore, because no superconductivity was seen in Sample C, which should contain more pure In, In_2Bi, and In_5Bi crystallites, this suggests that the superconductivity observed in Sample D comes from the InBi phase. Previous studies of InBi superconductivity have suggested that the T_c was less than 1.5 K[33] but could be raised up to 3.5 K at 10 GPa of pressure.[35] The higher T_c observed here for Sample D compared to bulk-synthesized InBi crystals could either be from higher carrier concentrations, higher InBi crystallite quality, or strain within the films.

IV. CONCLUSION

Coalesced InBi films on high-resistivity Si(111) substrates by molecular beam epitaxy have been attained. The indium flux during growth was responsible for large variations in morphology, crystal structure, temperature-dependent transport, and carrier concentration. The highest-quality InBi epitaxial layer, grown with a Bi:In flux ratio of 4.84, coalesced in the tetragonal InBi phase with a smooth, epitaxial interface on the Si(111). These InBi layers are comparable to Bi in terms of temperature-dependent resistivity but have smaller magnetoresistance, higher carrier concentrations, and potentially more complex Fermi surfaces. Bi-rich InBi films displayed single-phase dominated superconductivity with a T_c higher than previously seen for the InBi phase at atmospheric pressure.

ACKNOWLEDGMENTS

This material is based upon work supported by the National Science Foundation (NSF) under Grant Nos. DGE-1650441, E2CDA ECCS-1740286, and EFRI NewLAW EFMA-1741694 and was partially supported by the Semiconductor Research Corporation as nCORE task 2758. This work was performed in part at the user facilities supported by NSF (No. DMR-1719875).

REFERENCES

[1]L. Shubnikov and W. J. de Haas, Commun. Phys. Lab. Leiden, Report Nos. 207a, 207b, 207c, 207d, 210a, 210b (1930).
[2]W. J. de Haas and P. M. van Alphen, Commun. Phys. Lab. Leiden, Report Nos. 212a, 220d (1930).
[3]N. Xu, Y. Xu, and J. Zhu, npj Q. Mater. **2**, 51 (2017).
[4]L. Fu and C. L. Kane, Phys. Rev. B **76**, 1 (2007).
[5]H. Zhang, C.-X. Liu, X.-L. Qi, X. Dai, Z. Fang, and S.-C. Zhang, Nat. Phys. **5**, 438 (2009).
[6]A. R. Mellnik, J. S. Lee, A. Richardella, J. L. Grab, P. J. Mintun, M. H. Fischer, A. Vaezi, A. Manchon, E.-A. Kim, N. Samarth, and D. C. Ralph, Nature **511**, 449 (2014).
[7]Y. Niimi, Y. Kawanishi, D. H. Wei, C. Deranlot, H. X. Yang, M. Chshiev, T. Valet, A. Fert, and Y. Otani, Phys. Rev. Lett. **109**, 156602 (2012).
[8]X. Wang, G. Bian, C. Xu, P. Wang, H. Hu, W. Zhou, S. A. Brown, and T.-C. Chiang, Nanotechnology **28**, 395706 (2017).
[9]S. Tixier, M. Adamcyk, T. Tiedje, S. Francoeur, A. Mascarenhas, P. Wei, and F. Schiettekatte, Appl. Phys. Lett. **82**, 2245 (2003).
[10]J. N. Baillargeon, K. Y. Cheng, G. E. Hofler, P. J. Pearah, and K. C. Hsieh, Appl. Phys. Lett. **60**, 2540 (1992).
[11]M. S. M. Weyers, Appl. Phys. Lett. **62**, 1396 (1993).
[12]D. G. Thomas, J. J. Hopfield, and C. J. Frosch, Phys. Rev. Lett. **15**, 857 (1965).
[13]F. A. Trumbore, M. Gershenzon, and D. G. Thomas, Appl. Phys. Lett. **9**, 4 (1966).
[14]K. Wang, Y. Gu, H. F. Zhou, L. Y. Zhang, C. Z. Kang, M. J. Wu, W. W. Pan, P. F. Lu, Q. Gong, and S. M. Wang, Sci. Rep. **4**, 5449 (2015).
[15]X. Y. Wu, K. Wang, W. W. Pan, P. Wang, Y. Y. Li, Y. X. Song, Y. Gu, L. Yue, H. Xu, Z. P. Zhang, J. Cui, Q. Gong, and S. M. Wang, Semicond. Sci. Technol. **30**, 94014 (2015).
[16]H. Okamoto and K. Oe, Jap. J. Appl. Phys. **37**, 1608 (1998).
[17]E. C. Young, M. B. Whitwick, T. Tiedje, and D. A. Beaton, Phys. Status Solidi (c) **4**, 1707 (2007).
[18]T. Tiedje, E. Young, and A. Mascarenhas, Int. J. Nanotechnol. **5**, 963 (2008).
[19]G. Vardar, S. W. Paleg, M. V. Warren, M. Kang, S. Jeon, and R. S. Goldman, Appl. Phys. Lett. **102**, 042106 (2013).
[20]J. A. Steele, R. A. Lewis, J. Horvat, M. J. B. Nancarrow, M. Henini, D. Fan, Y. I. Mazur, M. Schmidbauer, M. E. Ware, S.-Q. Yu, and G. J. Salamo, Sci. Rep. **6**, 28860 (2016).
[21]Y. Song, S. Wang, I. S. Roy, P. Shi, A. Hallen, and Z. Lai, J. Cryst. Growth **378**, 323 (2013).
[22]H. Koch, I. Pietzonka, B. Galler, M. Strassburg, H. Kalisch, A. Vescan, and H.-J. Lugauer, J. Cryst. Growth **414**, 42 (2015).
[23]M. Ferhat and A. Zaoui, Phys. Rev. B **73**, 115107 (2006).
[24]F.-C. Chuang, L.-Z. Yao, Z.-Q. Huang, Y.-T. Liu, C.-H. Hsu, T. Das, H. Lin, and A. Bansil, Nano Lett. **14**, 2505 (2014).
[25]L.-Z. Yao, C.-P. Crisostomo, C.-C. Yeh, S.-M. Lai, Z.-Q. Huang, C.-H. Hsu, F.-C. Chuang, H. Lin, and A. Bansil, Sci. Rep. **5**, 15463 (2015).
[26]Y. Ma, X. Li, L. Kou, B. Yan, C. Niu, Y. Dai, and T. Heine, Phys. Rev. B **91**, 235306 (2015).
[27]C.-P. Crisostomo, L.-Z. Yao, Z.-Q. Huang, C.-H. Hsu, F.-C. Chuang, H. Lin, M. A. Albao, and A. Bansil, Nano Lett. **15**, 6568 (2015).
[28]Y. Zhang, H. Ye, Z. Yu, H. Gao, and Y. Liu, RSC Adv. **8**, 7022 (2018).
[29]L. Nicolaï, J. Minár, J.-M. Mariot, U. Djukic, M.-C. Richter, O. Heckmann, T. Balasubramanian, M. Leandersson, J. Sadowski, J. Braun, H. Ebert, J. Denlinger, I. Vobornik, J. Fujii, M. Gmitra, and K. Hricovini (2018), e-print arXiv:1806.03061.
[30]Y. Zhang, Q. Xu, K. Koepernik, J. Gooth, J. van den Brink, C. Felser, and Y. Sun (2018), e-print arXiv:1805.12049.

[31]S.-A. Ekahana, S.-C. Wu, J. Jiang, K. Okawa, D. Prabhakaran, C.-C. Hwang, S.-K. Mo, T. Sasagawa, C. Felser, B. Yan, Z. Liu, and Y. Chen, New J. Phys. **19**, 065007 (2017).
[32]E. Trushin and A. Görling, Phys. Rev. Lett. **120**, 146401 (2018).
[33]R. E. Jones and W. B. Ittner, Phys. Rev. **113**, 1520 (1959).
[34]H. Ullmaier, R. H. Kernohan, E. Cruceanu, and E. Hering, J. Low Temp. Phys. **5**, 71 (1971).
[35]V. G. Tissen, V. F. Degtyareva, M. V. Nefedova, E. G. Ponyatovskii, and W. B. Holzapfel, J. Phys. Condens. Matter **10**, 7303 (1998).
[36]K. Nishimura, Phys. B Condens. Matter **329-333**, 1399 (2003).
[37]A. C. Gandhi and S. Y. Wu, Sci. Rep. **7**, 9442 (2017).
[38]V. Bhatt and C. Desai, Acta Metall. **28**, 933 (1980).
[39]B. Keen, R. Makin, P. A. Stampe, R. J. Kennedy, S. Sallis, L. J. Piper, B. McCombe, and S. M. Durbin, J. Electronic Mater. **43**, 914 (2014).
[40]C.-H. Hsu, Z.-Q. Huang, C.-Y. Lin, G. M. Macam, Y.-Z. Huang, D.-S. Lin, T. C. Chiang, H. Lin, F.-C. Chuang, and L. Huang, Phys. Rev. B **98**, 121404 (2018).
[41]C.-Y. Lin, C.-H. Hsu, Y.-Z. Huang, S.-C. Hsieh, H.-D. Chen, L. Huang, Z.-Q. Huang, F.-C. Chuang, and D.-S. Lin, Sci. Rep. **9**, 756 (2019).
[42]H. Okamoto, *ASM Handbook: Alloy Phase Diagrams* (ASM International, 1992), pp. 491–492.
[43]I. A. Lapkina, O. V. Sorokina, and V. V. Ufimtsev, Russian J. Inorg. Chem. **31**, 117 (1986).
[44]B. C. Giessen, M. Morris, and N. J. Grant, Trans. Metallurgical Soc. AIME **239**, 883 (1967).
[45]K. Okawa, M. Kanou, H. Namiki, and T. Sasagawa, Phys. Rev. Mater. **2**, 124201 (2018).
[46]C. R. Ast and H. Höchst, Phys. Rev. Lett. **87**, 177602 (2001).
[47]T. Hirahara, T. Nagao, I. Matsuda, G. Bihlmayer, E. V. Chulkov, Y. M. Koroteev, P. M. Echenique, M. Saito, and S. Hasegawa, Phys. Rev. Lett. **97**, 146803 (2006).
[48]Y. Ohtsubo, L. Perfetti, M. O. Goerbig, P. L. Fèvre, F. Bertran, and A. Taleb-Ibrahimi, New J. Phys. **15**, 033041 (2013).
[49]O. Prakash, A. Kumar, A. Thamizhavel, and S. Ramakrishnan, Science **355**, 52 (2017).